



**HAL**  
open science

## Description of Bandgaps Opening in Chiral Phononic Crystals by Analogy with Thomson scattering

Wei Ding, Tianning Chen, Chen Chen, Dimitrios Chronopoulos, Badreddine Assouar, Yongzheng Wen, Jian Zhu

► **To cite this version:**

Wei Ding, Tianning Chen, Chen Chen, Dimitrios Chronopoulos, Badreddine Assouar, et al.. Description of Bandgaps Opening in Chiral Phononic Crystals by Analogy with Thomson scattering. *New Journal of Physics*, 2023, 25 (10), pp.103001. 10.1088/1367-2630/acfc5e . hal-04271581

**HAL Id: hal-04271581**

**<https://hal.science/hal-04271581>**

Submitted on 6 Nov 2023

**HAL** is a multi-disciplinary open access archive for the deposit and dissemination of scientific research documents, whether they are published or not. The documents may come from teaching and research institutions in France or abroad, or from public or private research centers.

L'archive ouverte pluridisciplinaire **HAL**, est destinée au dépôt et à la diffusion de documents scientifiques de niveau recherche, publiés ou non, émanant des établissements d'enseignement et de recherche français ou étrangers, des laboratoires publics ou privés.



Distributed under a Creative Commons Attribution 4.0 International License

# Description of Bandgaps Opening in Chiral Phononic Crystals by Analogy with Thomson scattering

*Wei Ding<sup>1</sup>, Tianning Chen<sup>1</sup>, Chen Chen<sup>1</sup>, Dimitrios Chronopoulos<sup>2</sup>, Badreddine Assouar<sup>3</sup>, Yongzheng Wen<sup>4</sup>, Jian Zhu<sup>1,5\*</sup>*

<sup>1</sup>*School of Mechanical Engineering and State Key Laboratory of Strength & Vibration of Mechanical Structures, Xi'an Jiaotong University, Xi'an, Shaanxi 710049, P.R. China*

<sup>2</sup>*Department of Mechanical Engineering & Mechatronic System Dynamics (LMSD), KU Leuven, 9000, Belgium*

<sup>3</sup>*Université de Lorraine, CNRS, Institut Jean Lamour, F-54000 Nancy, France*

<sup>4</sup>*Key Laboratory of New Ceramics and Fine Processing, School of Materials Science and Engineering, Tsinghua University, Beijing, 100084, China*

<sup>5</sup>*School of Mechanical Engineering and State Key Lab of Digital Manufacturing Equipment & Technology, Huazhong University of Science and Technology, Wuhan, Hubei, 430074, P. R. China*

## Abstract

Chiral phononic crystals provide unique properties not offered by conventional metamaterial based on classic Bragg scattering and local resonance. However, it is insufficient to only consider the inertial amplification effect to describe its bandgap mechanism due to the absence of the bandgap caused by the chirality in some specific chiral structures. Here, we theoretically and experimentally introduce an analogy with Thomson scattering in electromagnetic waves to characterize the bandgap phenomena in chiral phononic crystals with translation-rotation coupling. Another phononic structures with translation-translation coupling are proposed to illustrate the universality of the analogy. We evidence that the coupling motion in chiral unit cells is similar to the result of Thomson scattering, which quantitatively formulizing as inertial amplification in theory and, twice elastic Thomson scattering allows the waves in the same polarization mode to superpose in antiphase, which is essence of the bandgap formation. This finding sheds a new light on the physics of the elastodynamic wave manipulation in chiral phononic crystals, thus opening a definite route for the pragmatic exploitation of chiral phononic crystals as well as other structures with motion coupling in achieving low-frequency and broad bandgaps.

## 1. Introduction

Phononic crystals (PnCs), one artificial periodical structure with the capability of flexible manipulation of acoustic and elastic waves, have received much attention[1-3]. The remarkable feature, i.e. the bandgap, provides a powerful ability to control the wave propagation, such as the design of the non-

1 reciprocal device [4-6] and the recent valley state formation with Dirac points degeneracy operation  
2 in its bandgap [7, 8].

3 Local resonance [9] and Bragg scattering [10] are regarded as the mainstream bandgap mechanisms.  
4 In essence, both mechanisms mean two methods of realizing destructive interference. For the  
5 distinction, the destructive interference of the former features by the opposite movements between the  
6 main structure and resonant subsystem [11-14]. Therefore, we can observe the negative mass or the  
7 negative stiffness from a macro perspective. For the latter, in classical Bragg scattering, the destructive  
8 interferences are caused by the distance difference that satisfies  $\lambda/2$  ( $\lambda$  is one wavelength) [15, 16].  
9 Distinguished from electromagnetic Bragg scattering, elastic waves are matter waves and their  
10 propagation relies on the vibration of the matter. Therefore, for elastic Bragg scattering, the tailored  
11 matrix can constrain the wave-propagation path. As a result, the bandgaps don't meet the principle of  
12 the classical Bragg scattering as shown in Eq. (1) [17-19], called deep sub-wavelength bandgaps. In  
13 other words, as long as realizing the destructive interferences in the propagation path, a bandgap would  
14 be available.

$$2 a \sin \theta = \lambda \quad (1)$$

16 Independent of local resonance and Bragg scattering gap, there is a design method called inertial  
17 amplification [20]. Ideally, its dynamic inertia can be amplified to infinity [20, 21]. Therefore, the  
18 disadvantages of local resonance and Bragg scattering, i.e., low frequency and broad band are  
19 incompatible with high stiffness and lightweight, can be overcome by this bandgap [20, 22-25].  
20 Although some remarkable advances have been achieved [26-30], the structure configurations with  
21 inertial amplification effect always originate from the classic geometric model to extend their  
22 versatility and applicability [26-28, 31], rather than for further progress in amplifying dynamic inertia.  
23 Eventually, the breakthrough in low-frequency bandgaps is stalled, which can be attributed to the lack  
24 of diverse structures superficially. Actually, the ultimate reason is the obscurity in the underlying  
25 physics of the bandgap. In detail, despite the existence of the inertial amplification (see Supplementary  
26 S1 and S2 or the reference [25]) in the system, the bandgap formation cannot be ensured in different  
27 geometrical configurations [24, 25, 32, 33]. Therefore, it deserves to study the essence of the inertial  
28 amplification and the underlying physics of this bandgap, to guide the advances of geometric  
29 diversification and thus provide more possible in lower-frequency bandgaps [26, 29, 31, 34].

1 In this work, we theoretically and experimentally investigate the wave phenomena and bandgap  
2 generation in the compression-torsion coupled PnCs to concretize the bandgap mechanism. An  
3 incident wave polarizing in one mode passing the chiral subunit cells will be decomposed into the  
4 outgoing waves with two polarizations, the one in translation and the other in rotation. The  
5 decomposition of the polarization can be considered as a splitting process of the incident waves, which  
6 can be an analogy to the result of Thomson scattering in electromagnetic waves [35] to be distinct from  
7 Bragg scattering [36]. It demonstrates that a minimum of twice Thomson scattering and the outgoing  
8 waves vibrating in identical mode have opposite phases after the second Thomson scattering are  
9 required to generate a bandgap. The findings are verified in a kind of chiral PnCs with translation-  
10 rotation coupling. For the universality of the underlying physics, another non-chiral lattice with the  
11 translation-translation coupling is proposed to demonstrate that this bandgap is not unique to chiral  
12 lattices but available in other lattices with Thomson scattering effects.

## 13 **2. Structure and results**

14 Fig. 1 shows the schematics of the unit cells and calculated band structures. The lattices in Fig. 1(a)  
15 and Fig. 1(b) are unit cells with translation-rotation coupling, and in Fig. 1(c) and Fig. 1(d) are unit  
16 cells with translation-translation coupling. Each type of lattice consists of two subunit cells. As  
17 depicted in Fig. 1(a) and 1(b), the arrayed translation-rotation coupling unit cell named ATR consists  
18 of two subunit cells **I**. The mirrored translation-rotation coupling unit cell called MTR consists of  
19 subunit cells **I** and **II**. The right panels in Figs. 1(a)-1(b) represent the corresponding band structure  
20 calculated by utilizing finite-element method-based software COMSOL Multiphysics. In terms of the  
21 bandgap, there is an extensive bandgap in MTR but not available in ATR.

22 In fact, the study on such bandgaps in MTR can be traced back to Bergamini's work in 2019 [25],  
23 where the bandgap mechanism is attributed to inertial amplification and the nature of the coupling  
24 between the spins of the atoms which is provided by the relative orientation of adjacent chiral centers.  
25 As revealed by Eq. (S58) and Eq. (S63) in Supplementary S2, the inertial matrixes of MTR and ATR  
26 have the inertial amplification effect, but the bandgap only exists in MTR. In other words, the current  
27 definition of inertial amplification lacks the universality principle of one mechanism like Bragg  
28 scattering and local resonance, even though inertial amplification has been studied for almost two  
29 decades. Therefore, this study aims to elucidate the underlying physics of inertial amplification and  
30 the coupling between the spins of the atoms.

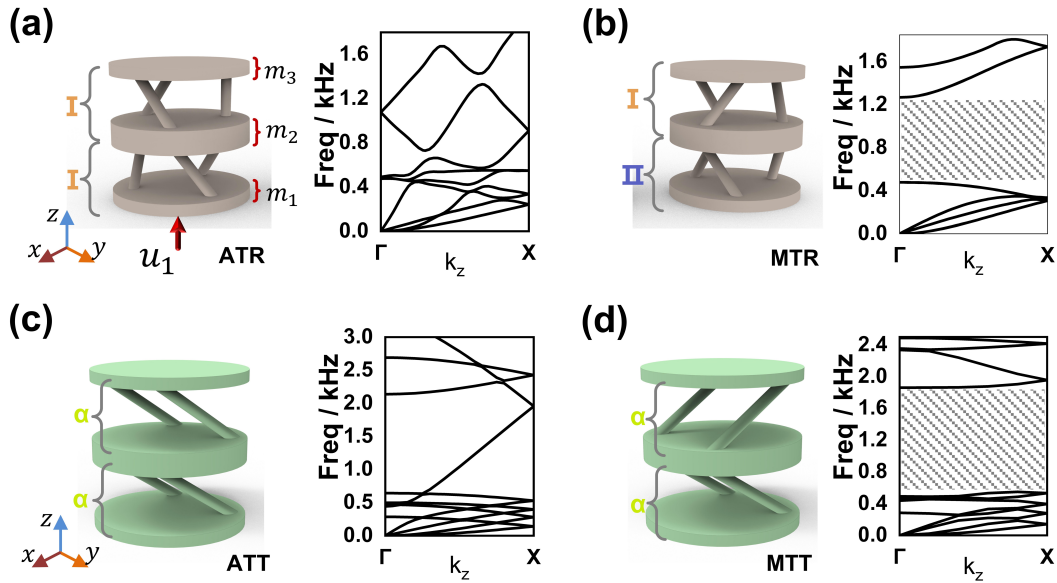


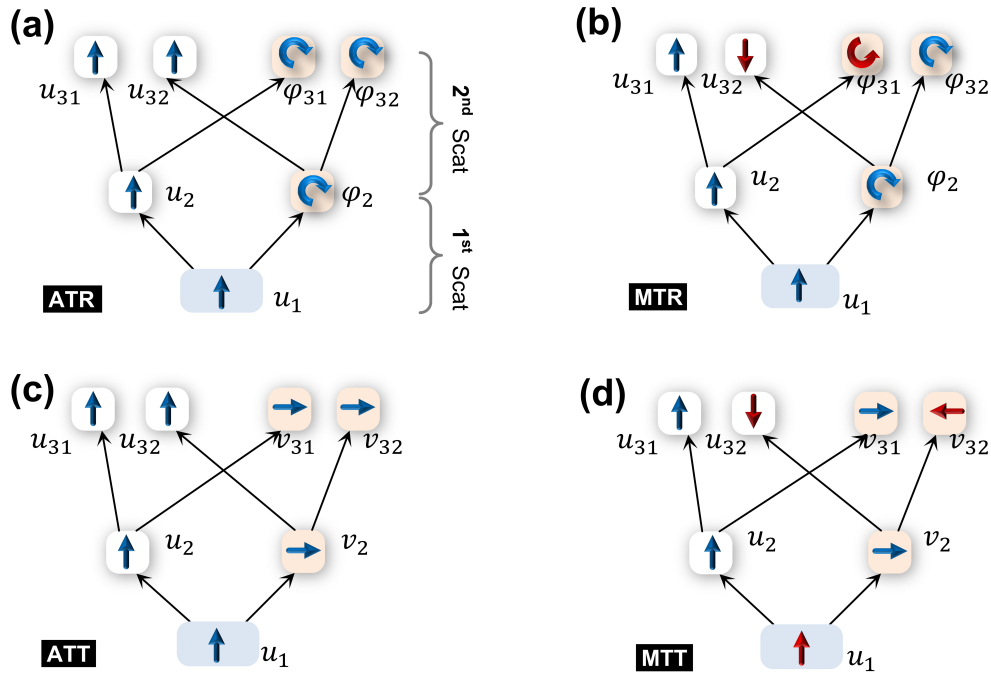
**Fig. 1. The lattices and the band structures. (a) Arrayed translation-rotation coupling unit cell (ATR); (b) Mirrored translation-rotation coupling unit cell (MTR); (c) Arrayed translation-translation coupling unit cell (ATT); (d) Mirrored translation-translation coupling unit cell (MTT). As denoted in (a), each disk represents an individual lumped mass  $m_i$ . The symbols “I” and “II” represent two different subunit cells of translation-rotation coupling lattices (More details of the geometry can refer to Fig. S1). The symbol “I” is left-handed, and the symbol “II” is right-handed. The symbol “ $\alpha$ ” is the subunit cell of translation-rotation coupling lattices, and its geometry is illustrated in Fig. S7.). The right panels in (a)-(d) represent the corresponding band structure with the bandgaps highlighted by gray areas.**

As illustrated in the analysis of the subunit cell I (more details in Supplementary S1), the chiral effect essentially achieves the motion coupling and thus exhibits the function of the inertial amplification, but this is not sufficient to form a bandgap. Due to the ambiguous contribution of chirality to the bandgap generation, one may easily attribute the underlying physics of the bandgap in Fig. 1(b) to the chirality. For instance, in some specific functional structures, chirality can indeed bring novel phenomena [37], such as negative Poisson’s ratio [38], high structural damping [39], and spin mechanical metastructures [40]. Some of these aforementioned properties have been realized in other non-chiral structures [17, 41, 42]. Therefore, chirality is one of the effective ways but not the exclusive way to achieve the desired function.

The designed non-chiral unit cells with translation-translation coupling consist of two subunit cells  $\alpha$  are demonstrated in Fig. 1(c) and Fig. 1(d). The arrayed and mirrored translation-translation coupling

1 unit cell with central and rotational symmetry in  $\alpha$  is named ATT and MTT. The right panels in Fig.  
 2 1(c)-1(d) represent the calculated band structure. From the perspective of the bandgap, there is a  
 3 phenomenon similar to that between MTR and ATR in Fig. 1(a)-1(b), i.e., MTT has a bandgap that is  
 4 not in ATT, which is an encouraging result as it confirms that the bandgap possessed in MTR is not  
 5 exclusive to chiral lattices.

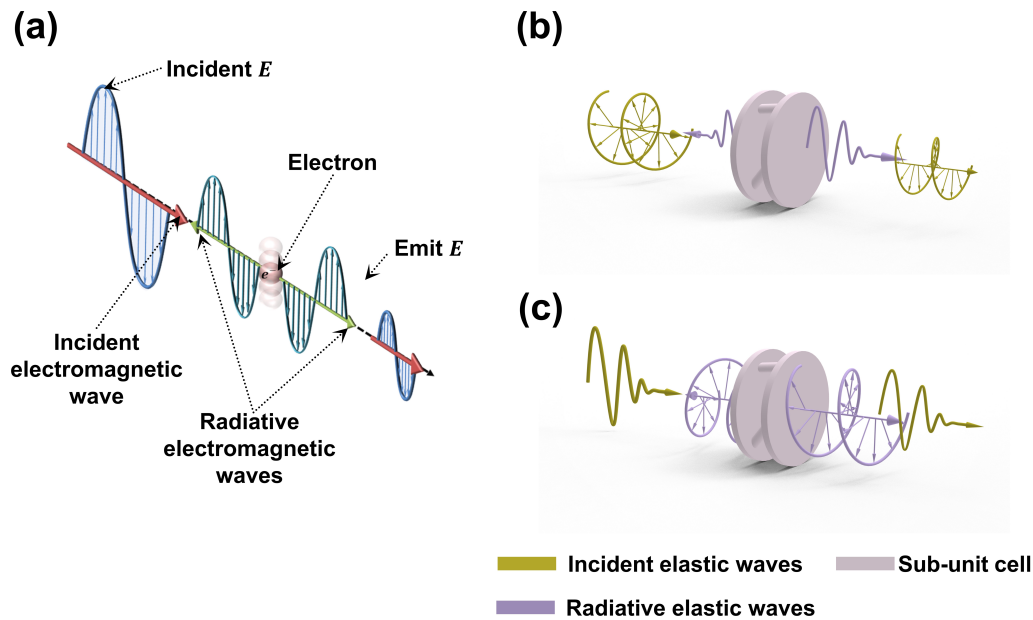
### 6 3. Mechanism analysis



7

8 **Fig. 2. The decomposition of the movement for (a) ATR, (b) MTR, (c) ATT, and (d) MTT.  $u_i$  and  $\varphi_i$  is**  
 9 **the corresponds to the  $i^{th}$  lumped mass, as denoted in Fig. 1(a). The abbreviation “Scat” refers to**  
 10 **scattering.**

11 To elucidate the mechanism of the bandgap generation, Fig. 2 shows the initial polarization  
 12 orientations of the oscillators when the wave propagates in four types of unit cells shown in Fig. 1. For  
 13 the sake of simplicity, two assumptions are made during the analysis. The z-axis rotational freedom of  
 14  $m_1$  is restricted; the incident wave vibrates sinusoidally in translational form, and the initial direction  
 15 of vibration is along +z axis with an initial phase of zero (refer to the coordinate system shown in Fig.  
 16 1). As shown in Fig. 2(a) or Fig. 2(b), when the incident wave passes through the first subunit cell, the  
 17 translation  $u_1$  will split into the translation  $u_2$  and rotation  $\varphi_2$ .



1

2 **Fig. 3. (a) Diagram of the classical electromagnetic Thomson scattering. (b) The scattering diagram of**  
 3 **the translational polarization in chiral sub-unit cells when the input is rotational polarization. (c) The**  
 4 **scattering diagram of the rotational polarization in chiral sub-unit cells when the input is translational**  
 5 **polarization. The translational polarization in (b) and (c) strictly is longitudinal. For clarity, we use the**  
 6 **shear linear polarization to replace it. (Refer to Supplementary S7 for more details on the numerical**  
 7 **data).**

8 Actually, the splitting process of the polarization is similar to the Thomson scattering. As illustrated  
 9 in Fig. 3(a), in classical Thomson scattering, the plane electromagnetic wave forces the electron to  
 10 vibrate; the vibration of electrons will create a harmonic electric field, thus resulting in two  
 11 electromagnetic waves with the same frequency as the incident wave, which propagate in two  
 12 directions [35]. For simplicity, we defined the torsional harmonic as rotational polarization. In our  
 13 analogue, the subunit cell is regarded as the electron; as shown in Fig. 3(b) (Please refer to the results  
 14 of the time domain simulation in **Supplementary S7** for more details), if the input is translational  
 15 polarization, the subunit cell will vibrate in linear polarization but radiate another component wave  
 16 which vibrates in rotational polarization; conversely, when the input is the rotational polarization, the  
 17 radiative wave will vibrate in translational polarization.

18 One can see some similarities between the process of the classical Thomson scattering (Fig. 3(a)) and  
 19 the wave propagation in the models (Fig. 3(b) and Fig. 3(c)). In terms of the function, the compression-

torsion feature of the subunit cell is similar to the charged property of the electron in Thomson scattering. In terms of the scattering process, the forced vibration of the electrons driven by the incident electromagnetic wave is similar to the vibration of the subunit cell driven by the incident elastic wave. From the results, the translational radiated waves in Fig. 3(b) and the rotational radiated waves in Fig. 3(c) are dipoles, which resembles the phenomenon of classical Thomson scattering shown in Fig. 3(a). The change of the wavefront in classical Thomson scattering is a superimposing effect of scattered waves propagating in multiple directions [43, 44]. However, limited by the layout of the chiral subunit cell, the scattered waves cannot diverge to infinite space like the classical Thomson scattering but can only propagate in the direction of the periodical structure. These similarities enable us to draw an analogy with Thomson scattering to clarify the process of wave propagation in chiral subunit cells. Therefore, for simplicity, we name the wave propagation process in the chiral subunit cell as Thomson scattering.

Furthermore, the process that these scattered waves ( $u_2$  and  $\varphi_2$ ) pass through the second subunit cell is equivalent to undergoing a second Thomson scattering. The distinction from the first is that the second scattering has two incident waves ( $u_2$  and  $\varphi_2$ ). Consequently, after the second scattering, it will produce four scattered waves, i.e.,  $u_{31}$ ,  $u_{32}$ ,  $\varphi_{31}$ , and  $\varphi_{32}$ . Among them,  $u_{31}$  and  $u_{32}$  vibrate in translation, but  $\varphi_{31}$  and  $\varphi_{32}$  vibrate in rotation.

In ATR, by the first scattering, the initial direction of the scattered waves  $u_2$  and  $\varphi_2$  are  $+z$  and clockwise around the  $+z$  axis (from the  $+z$ -axis perspective), respectively. After the second scattering, regarding  $u_2$  as the incident wave, the initial direction of the scattered wave  $u_{31}$  is  $+z$ , and the initial direction of the scattered wave  $\varphi_{31}$  is in the clockwise direction. Meanwhile, regarding  $\varphi_2$  as the incident wave, the initial direction of  $u_{32}$  is  $+z$ , and the initial direction of  $\varphi_{32}$  is also in the clockwise direction. Since the two translations  $u_{31}$  and  $u_{32}$ , and the two rotations  $\varphi_{31}$  and  $\varphi_{32}$  have the same direction,  $u_3$  and  $\varphi_3$  of  $m_3$  in ATR can be written as Eq. (1) and Eq. (2).

$$u_3 = u_{31} + u_{32}. \quad (1)$$

$$\varphi_3 = \varphi_{31} + \varphi_{32}. \quad (2)$$

Eventually, the absolute angle  $\varphi_3$  of  $m_3$  in ATT can be determined as

$$\varphi_3 = q(u_1 - u_3), \quad (3)$$

where  $q$  is the rotational angle of translation per unit (see Supplementary S2 for details).

Conversely, in MTR, the initial direction of the scattered wave  $u_{31}$  is +z, and the initial direction of the scattered wave  $\varphi_{31}$  is in the clockwise direction; nevertheless, the initial direction of  $u_{32}$  is -z, and the initial direction of  $\varphi_{32}$  is in the counterclockwise direction. The  $u_3$  and  $\varphi_3$  of  $m_3$  in MTR can be written as

$$u_3 = u_{31} - u_{32} \quad (4)$$

and

$$\varphi_3 = \varphi_{31} - \varphi_{32}. \quad (5)$$

Then, in MTR, the absolute angle  $\varphi_3$  can be determined as

$$\varphi_3 = q(u_1 + u_3 - 2u_2). \quad (6)$$

The difference in the absolute angle for  $m_3$  in ATR and MTR leads to the immense variability of the elements in inertial matrixes  $\mathbf{M}$  and  $\mathbf{M}'$  in Eq. (7) (more details in Supplementary S2). Detailly, for instance, for the inertial matrix for ATR,  $\mathbf{M}$  is written as

However, for the inertial matrix for MTR,  $\mathbf{M}$  is written as

In brief, after twice Thomson scattering, the property that the scattered waves vibrating in the same modes have opposite initial vibration directions similar in MTR plays a decisive role in the presence of the bandgap.

$$\mathbf{M}\ddot{\mathbf{u}} + \mathbf{K}\mathbf{u} = \mathbf{M}'\ddot{\mathbf{u}}_1 + \mathbf{K}'\mathbf{u}_1. \quad (7)$$

The splitting process and wave propagating in the translation-translation coupling (ATT and MTT) PnCs can also be an analogy to Thomson scattering, as shown in Fig. 2(c) and Fig. 2(d). In ATT, by the first scattering, the initial directions of the scattered waves  $u_2$  and  $v_2$  point in +z and +x axis.  $u_{31}$ ,  $u_{32}$  and  $v_{31}$ ,  $v_{32}$  point to +z and +x directions after the second scattering when  $u_2$ ,  $v_2$  are considered as the incident wave. However, in MTT,  $u_{31}$  and  $u_{32}$  point to +z and -z,  $v_{31}$  and  $v_{32}$  point to -x and +x directions, respectively. The superposition of these waves in MTT with opposite vibrating directions enables the capability of energy cancellation and generating bandgap, coinciding with the

findings in MTR. Therefore, the analogy results confirm the universality of the mechanism proposed in this work.

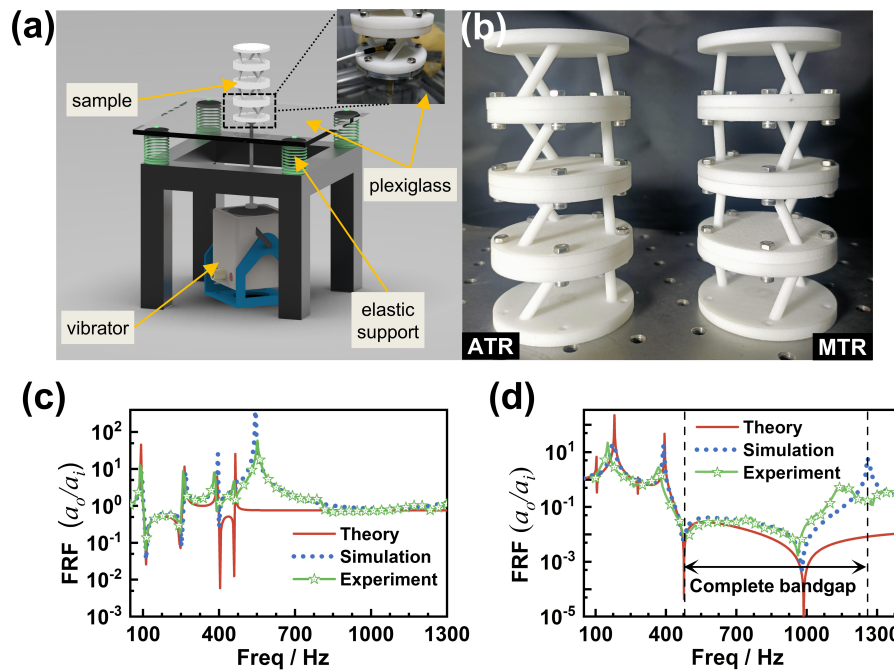
#### 4. Theoretical, numerical, and experimental verification

To verify the reasonability of the wave phenomena and bandgap feature described by using the analogy of Thomson scattering in Fig. 2, we have built the movement relationship in formulas according to the scattering process (more details of the theory in Supplementary S2). Meanwhile, the theoretical frequency response functions (FRFs) of the 2 unit cells in Fig. 4(b) are carried out, as displayed by the red solid lines in Fig. 4(c) and Fig. 4(d). From the theoretical results, at high frequencies, the FRFs of MTR and ATR are constant, but only the MTR exhibits significant attenuation, which allows the excellent potential for generating an ultra-broad bandgap in this lattice. Fig. 4(d) shows two anti-resonant notches, which facilitate enhancing the attenuation of bandgaps. Meanwhile, compared with the FRF in Figure S2, the theoretical result in Fig. 4(d) shows one more anti-resonance peak when the finite structure has two unit cells, which means that the number of the anti-resonance notches can be increased with the increase of the number of the unit cell. This property will be further discussed in Section 5.

To demonstrate the correction of the theory, the finite-period structures containing 2 unit cells of ATR and MTR are numerically calculated in COMSOL solid mechanics module. The material is one kind of Nylon with the elastic modular  $E = 1.6 \times 10^9$  Pa, the Poison's ratio  $\nu = 0.4$ , and the density  $\rho = 1000$  kg/m<sup>2</sup>. In the simulation, only the z-axis translational freedom of the disk at the input end is reserved to match the boundary conditions of the theory. The surface displacement load is applied at the input end disk rather than a force load to ensure consistency with the analysis and experiment. The domain point probes record the acceleration signals  $a_i$  at the center of the input end lumped mass and  $a_o$  at the output end. The FRF can be calculated by taking  $a_i$  as the reference and the numerical results are presented as blue dotted lines in Fig. 4(c) and Fig. 4(d).

Fig. 4(a) shows the details of the experimental configuration, and Fig. 4(b) shows the fabricated ATR and MTR samples through photopolymerization-based 3D printing technology. The sample input disk is bolted to a plexiglass with a thickness of 10 mm. Notably, the plexiglass has approximately ten times weight than the two unit cells, to limit the freedom of rotation of the disk around the z-axis as much as possible. The plexiglass is supported using elastic supports to avoid exceeding the allowable amplitude

1 range to protect the shaker. Three foam pieces are used instead of the ideal elastic support to level the  
 2 plexiglass easily. The shaker is excited directly on the plexiglass through the top bar to simulate the  
 3 input of displacement load input in simulation and analysis. Two sensors (PCB 353B15) are attached  
 4 to the top and the bottom of the sample to pick up the output acceleration  $a_o$  and the input acceleration  
 5  $a_i$ , respectively. The experimental results obtained by the accelerometers are recorded in real-time  
 6 using M+P Vibpilot. The frequency range of the sine sweep is 100 Hz - 1500 Hz with a frequency  
 7 resolution of 2 Hz and the sweeping speed is 400 Hz/min, to guarantee the precision of experimental  
 8 data. The experimental FRFs are marked by the green line with stars.



9

10 **Fig. 4. (a) The schematic of the experimental configuration. The insert in the upper right corner is the**  
 11 **detail of the connection between the sample and the plexiglass. (b) Photograph of the investigated**  
 12 **samples. ATR sample on the left, and MTR sample on the right. (c) Experimental (green solid with stars),**  
 13 **numerical (blue dotted), and analytical (red solid) frequency response functions (FRFs) of ATR. (d)**  
 14 **Experimental (green solid with stars), numerical (blue dotted), and analytical (red solid) FRFs of MTR.**

15 As illustrated in Fig. 4(c) and 4(d), a significant attenuation occurs from 450 Hz to 1280 Hz in the FRF  
 16 of MTR, and it does not exist in that of ATR. In a nutshell, the bandgap does only exist in MTR, not  
 17 in ATR. Significantly, the consistency of experimental, numerical, and theoretical results demonstrates  
 18 the correctness of the analysis. Also, it verifies the validity of the analogy that the bandgap generation  
 19 mechanism of this PnC is similar to Thomson scattering. Limited by the insufficient degrees of the

freedom in the lumped mass method, the theoretical FRF at high frequency has a large discrepancy with numerical and experimental results, such as over 500 Hz for ATR and over 1000 Hz for MTR. Nevertheless, the intuitive nature of this method in bandgap-mechanism explanation is irreplaceable than other precise methods, such as spectral element method [45].

## 5. Discussion

### 5.1 Anti-resonant notches

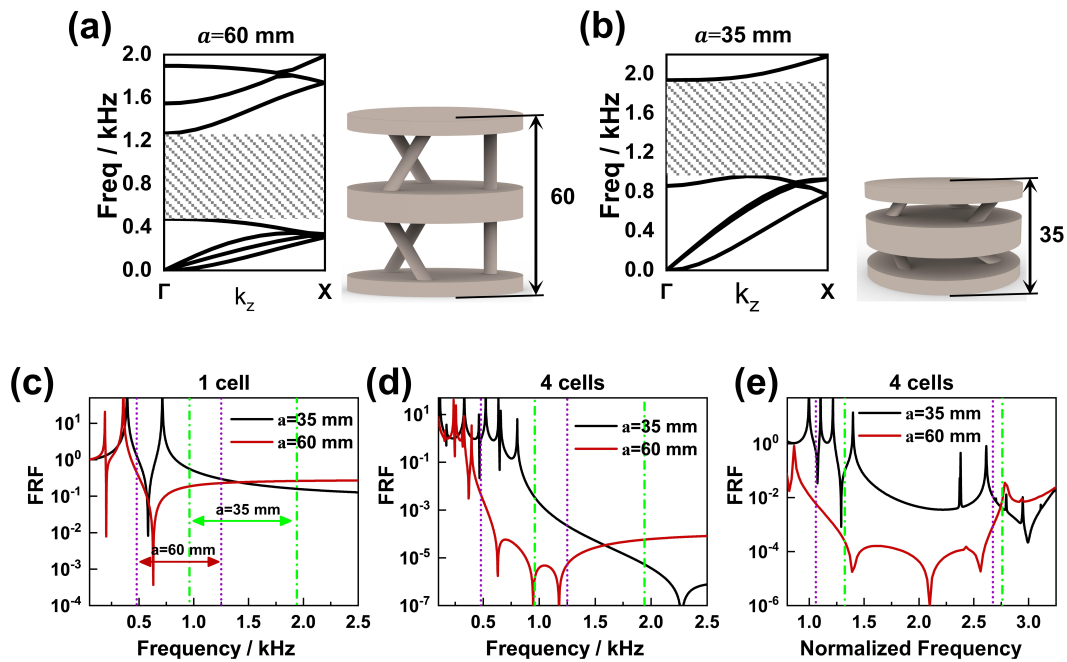


**Fig. 5.** The comparison of the MTR unit cells with  $a = 60$  mm and  $a = 35$  mm. (a) & (b) The band structures (left side) and the model schematics (right side) of the ones with  $a = 60$  mm and  $a = 35$  mm. (c) & (d) The analytical FRFs of MTR finite structures with the lattice constant  $a = 60$  mm and  $a = 35$  mm. (e) The numerical FRFs of MTR finite structures composed of 4 unit cells with the lattice constant  $a = 60$  mm and  $a = 35$  mm. The black dashes are the bandgap boundaries of  $a = 60$  mm and green lines are that of  $a = 35$  mm.

Previous studies [20, 30] mentioned that when the inertia is amplified, there will be an anti-resonant notch in FRF, and the anti-resonant notch can be observed in complex band structures [7, 34]. Although the inertial amplification is involved in the Thomson scattering-induced bandgap, the anti-resonant notch is unessential for forming the Thomson scattering-induced bandgap.

Fig. 5 shows the band structures of the MTRs with  $a = 60$  mm and  $a = 35$  mm. When the lattice constant is 60 mm, the bandgap is 480 Hz – 1250 Hz; when  $a = 35$  mm, it is 960 Hz – 1940 Hz. Fig. 5(c) and Fig. 5(d) show the analytical FRFs of MTR with different numbers of the unit cell when the lattice  $a = 35$  mm (blue line) and  $a = 60$  mm (red line). Because the lattice constant varies from 60 mm to 35 mm, the stiffness increases from 256060 N/m to 377630 N/m, and the amplified inertia decreases from 0.0432 to 0.0062 (Both variables are obtained theoretically). One can observe from Fig. 5(c) that the anti-resonant frequency disappears when  $a = 35$  mm. As shown in Fig. 5(d), despite the anti-resonant frequency appears again when the number of the unit cell is 4, the reduction of the amplified inertia leads to the shift of the anti-resonant frequencies toward higher frequency and even beyond the range of the bandgap.

To accurately catch the effect of the anti-resonant notches on the FRF, Fig. 5(e) shows the numerical FRFs of the finite structures with 4 unit cells. For comparison purposes, we consider the influence of the geometric configurations of the lattice constant and equivalent physical parameters on the FRF [22, 46], so we use Eq. (8) to normalize the frequency in FRFs.

$$f_n = \frac{fa}{\sqrt{\frac{k_{eff}}{\rho_e}}} \quad (8)$$

The filling ratio can be determined as

$$\rho_e = \frac{M}{V}, \quad (9)$$

where the parameter  $V$  can be calculated by

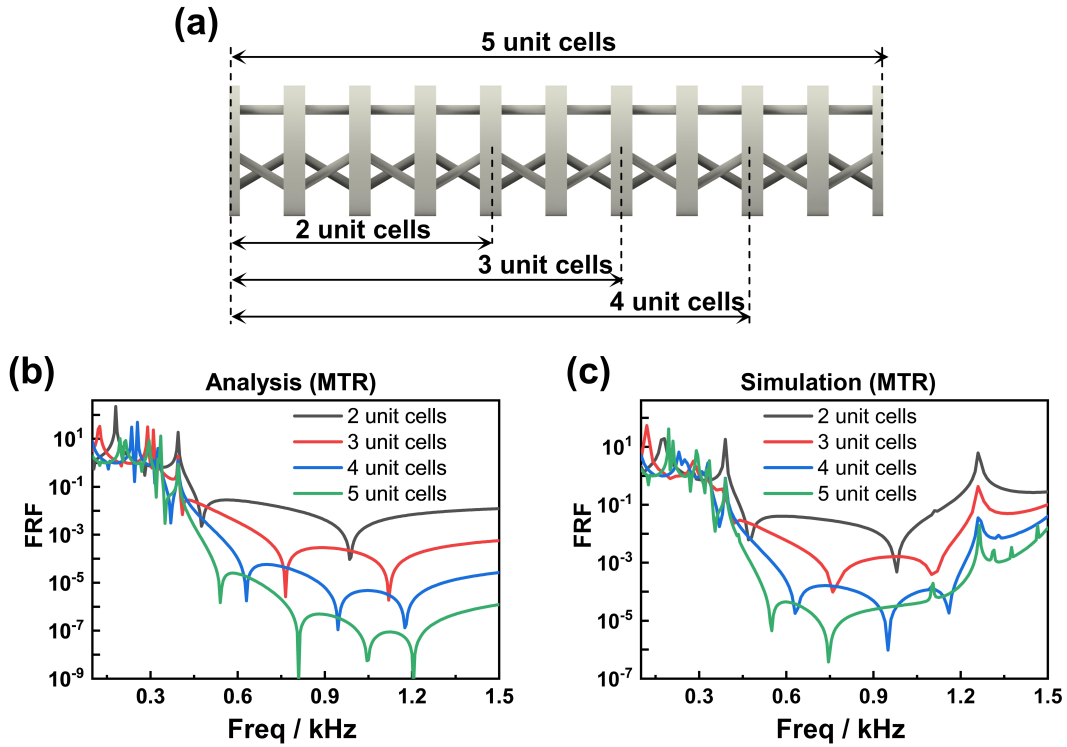
$$V = \frac{D^2\pi a}{4}. \quad (10)$$

The equivalent stiffness  $k_{eff}$  can be determined by Eq. (S14).

According to the analysis, the filling ratio is 586 kg/m<sup>3</sup> for  $a = 35$  mm, and it is 346.9 kg/m<sup>3</sup> for  $a = 60$  mm; the equivalent stiffness is equal to 377630 N/m for  $a = 35$  mm, and that is equal to 256060 N/m for  $a = 60$  mm. The normalized FRFs are shown in Fig. 5(e).

It can be observed from Fig. 5(e) that the depth of  $a=35$  mm is significantly weaker than that of  $a = 60$  mm when the anti-resonant notches disappear. When the number of periods is up to 4, the attenuation difference is even by more than two orders of magnitude. Most importantly, influenced by

1 the resonant frequency at the upper boundary, the theoretical anti-resonant frequency is not reflected  
 2 in the FRFs. Despite the disappearance of the anti-resonant notches, the bandgap is still reserved in the  
 3 band structure.



4

5 **Fig. 6. (a) Schematics of the finite structure with different numbers of the MTR unit cells. (b) Theoretical**  
 6 **and (c) numerical discussion about the variation of the anti-resonant notch with the number of the MTR**  
 7 **unit cells.**

8 Undeniably, the existence of anti-resonant notches has significant implications. Fig. 6(a) gives the  
 9 pattern of variation in the number of MTRs. As shown in Fig. 6(b), as the number of the unit cells  
 10 increases, the converged value at high frequency will decrease, and the number of the anti-resonant  
 11 notch will increase (These properties do not exist in ATR, please see Supplementary S4 for more  
 12 details). The increase in anti-resonant gaps can accelerate bandgap formation. Notably, the anti-  
 13 resonant notches are located mainly at the lower boundary of the bandgap and are spread, which  
 14 enhances the modulation capacity of low-frequency and broad elastic waves.

15 In fact, as shown in Fig. 6(b), the infinite extension of the attenuation will be cut off due to the higher-  
 16 frequency resonance modes. These resonant modes will suppress the anti-resonant notches close to it.

Therefore, the anti-resonant notches at high frequency will be covered with the number of periods increases, thus weakening the attenuation, as illustrated by the green plot in Fig. 6(a) and 6(b).

To sum up, the bandgap formation does not depend on the anti-resonant notch. The anti-resonance frequency just has the function of enhancing the manipulation of low-frequency. Determining the type of the bandgap by the shape of the attenuation is inaccurate [16, 47-49], especially for Bragg scattering-induced and Thomson scattering-induced bandgaps.

### ***5.2 Thomson scattering-induced and Bragg scattering-induced bandgaps***

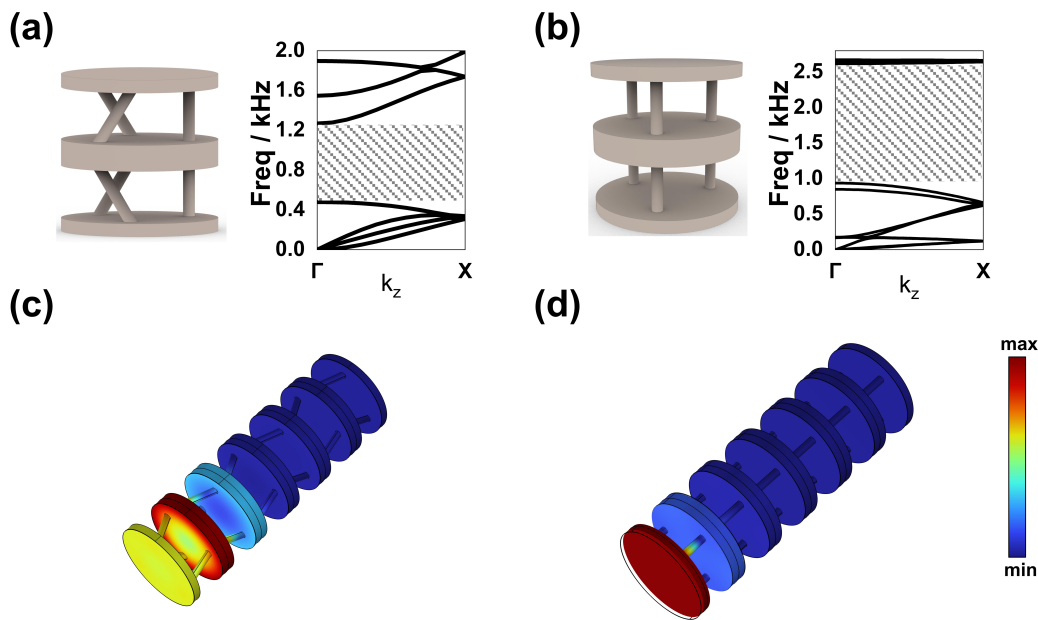
Fig. 7(a) and 7(b) exhibit a Thomson scattering unit cell and a Bragg scattering unit cell to find the intrinsic distinction between the Bragg scattering and Thomson scattering bandgaps. The parameter  $\theta$  of the MTR is set as  $90^\circ$  to invalidate the coupled motion and reserve the translation alone, thus allowing a Bragg scattering unit cell to be obtained, as shown in Fig. 7(b). Consequently, there is a Bragg scattering bandgap due to the impedance mismatch between the lumped masses and the ligaments [10, 50].

For a fair comparison, all physical parameters are the same except that the elasticity modulus of the ligaments in the Bragg scattering unit cell is determined to be  $1.05e8$  Pa to maintain the same stiffness between both unit cells in Fig. 7. Consequently, the equivalent stiffness and lattice constants of the cells are identical. There is a slight variation in the equivalent density of the unit cells because of the variation in ligament length. The total mass of the six ligaments in the MTR unit cell is 2.3 g, while the one in the Bragg scattering unit cell is 1.9 g (The total mass of the MTR unit cell is 58.86 g). Therefore, we named the condition quasi-equal density.

Under the condition of the same lattice constant, stiffness, and quasi-equal density, the Thomson scattering bandgap extends from 400 Hz to 1200 Hz with a relative width of 100% (as illustrated in Fig. 7(a)), while a Bragg scattering bandgap at 930 – 2610 Hz with a relative width of 95% can be observed in Fig. 7(b). A shift in the starting frequency to a lower frequency is evident, reaching 57% with 930 Hz as a reference.

From Fig. 7(c) and 7(d), significant variances in energy distributions of both types of bandgaps can be observed. In classical Thomson scattering, the forced vibration of the electron is the key to scattering. In the bandgap induced by the analogous Thomson scattering, it requires that the scattered waves undergone the first scattering needs to undergo the Thomson scattering again. In addition, the second-

1 round scattered waves polarized in the same mode must have opposite phases to achieve destructive  
 2 interference. It can be determined from this process that the involvement of the lumped masses is  
 3 crucial for achieving attenuation. Since the first lumped mass is the vibration source and the waves  
 4 have destructive interference in the process of the second scattering, the energy within the bandgap  
 5 should be mainly concentrated in the second lumped mass. Indeed, Fig. 7(c) verifies this reasoning.  
 6 However, in classical Bragg scattering, the interaction between the incident wave and the scatterer is  
 7 for reflecting incident waves. In Bragg scattering PnCs, the function of the scatterers is to reflect the  
 8 incident wave and thus produce destructive interference. Correspondingly, the energy of the Bragg  
 9 scattering bandgap is mainly localized in the matrix medium. For the unit cell of Fig. 7(b), the lumped  
 10 masses act as the scatterers and the ligaments act as the matrix. Therefore, the energy of the bandgap  
 11 should be mainly localized to the ligaments as the matrix medium, as can be observed in Fig. 7(d).



12

13 **Fig. 7. The comparison of the Thomson scattering-induced and Bragg scattering-induced bandgaps. (a)**  
 14 **The Thomson scattering unit cell and its band structure. (b) The Bragg scattering unit cell and its band**  
 15 **structure. Both unit cells have the same lattice constant, lumped masses, and equivalent stiffness. The**  
 16 **deformation profiles of the (c) Thomson scattering (at 800Hz) and (d) Bragg scattering finite structures**  
 17 **(at 1400 Hz).**

1 The analogy of Thomson scattering can reasonably explain several phenomena from the perspective  
2 of underlying physics. It is well known that Bragg scattering is the elastic collision between the waves  
3 and the atoms. The scattered waves in Bragg scattering rely on the heavy atoms to reflect the incident  
4 waves and thus to destructive interferences [51]. Thomson scattering depends on the polarization of  
5 electrons to generate divergent outgoing waves in different polarizations [36]. In the Bragg scattering  
6 lattice, the propagation of the scattered wave does not depend on the vibration of the scatterers  
7 represented by the lumped masses, and thus the scattered waves propagate mainly as reflections [51]  
8 with the vibration concentrated on the ligaments [15, 47]. In Thomson scattering, however, the  
9 propagation of the scattered waves depends on the polarization of the electrons represented by the  
10 entire subunit cell. The orientation of the scattered waves is primarily in the forward direction of the  
11 incident wave. As a result, the attenuation in the bandgap is gradient rather than localized on ligaments  
12 (please refer to Fig. S8). Because the electrons are much lighter in mass than the atoms, the Thomson  
13 scattering will produce a more lightweight unit cell than a Bragg scattering unit cell for the same lattice,  
14 stiffness, and bandgap starting frequency [52, 53], which can also be drawn from Fig. 7. In addition,  
15 Thomson scattering allows a smaller number of the periods to reflect the significant attenuation of the  
16 bandgap (please refer to Fig. 6).

## 17 **6. Conclusion**

18 In conclusion, we have theoretically and experimentally demonstrated the wave propagation and the  
19 formation mechanism of bandgaps in compression-rotation coupling PnCs. The coupling motion and  
20 wave propagation profile present an analogy to Thomson scattering. The results revealed that several  
21 conditions need to be met in the analogue Thomson scattering-based PnCs to generate a bandgap. First,  
22 the orthogonal coupling motions are essential for producing the Thomson scattering, which is  
23 quantitatively characterized as inertial amplification in equations. Second, these initial scattered waves  
24 must undergo a minimum of twice Thomson scattering. Third, the secondary scattered waves vibrating  
25 in the same mode should have the opposite initial direction of the vibration, which is the cause of the  
26 superimposable attenuation, and thus generates the bandgap. Remarkably, the third condition is the  
27 nature of that the inertial coupling phenomena (i.e. a non-diagonal inertial matrix as mentioned in Refs.  
28 [26, 30, 31] and Eq. (S58)) occurs in theory. Although the quantitative characterizations demonstrate  
29 the anti-resonant frequencies in FRFs, the anti-resonant frequency is not essential for the bandgap  
30 generation. This work revealed that PnCs with inertial amplification only cannot ensure an extensive

bandgap similar to MTR and MTT. Chirality is a virtual design element and one of the methods in realizing the Thomson scattering but not an indispensable condition for achieving such a bandgap. It should be emphasized, the analogue to classic Thomson scattering of electromagnetic waves was proposed to help us to understand the underlying physics of the bandgap. Indeed, the underlying physics of the bandgap in our work cannot be considered to be completely identical to the general mechanism (classic Thomson scattering). Both have some significant differences and are not limited by the fact that the extremely important aspect of the Thomson scattering is for the long-wavelength limit which is not considered in this analogue. Despite these, the materialization of the inertial amplification and bandgap generation carried out in this work enables to couple of any two or more orthogonal modes to generate a substantial inertial amplification (instead of by the law of leverage [26, 54]), and thus generate an ultra-low-frequency bandgap. The works could shed new light on the physics of the elastodynamic wave manipulation in inertial amplification-induced PnCs, and offer an entirely exotic avenue for the diverse design and investigation of PnCs with remarkable properties, such as the bandgap with lower starting frequency, broadband, and extensive attenuation.

## Acknowledgments

This work was financially supported by the National Natural Science Foundation of China (No. 12002258), the State Key Lab of Digital Manufacturing Equipment & Technology of HUST (DMETKF2021014), the Natural Science Foundation of Shaanxi Province (No. 2020JQ-043). Wei Ding is grateful for the support of the China Scholarship Council (Grant No. 202206280170).

## References

- [1] Wu L, Wang Y, Chuang K, Wu F, Wang Q, Lin W, et al. A brief review of dynamic mechanical metamaterials for mechanical energy manipulation. *Mater Today*. 2020;44:168-93.
- [2] Jia Z, Liu F, Jiang X, Wang L. Engineering lattice metamaterials for extreme property, programmability, and multifunctionality. *J Appl Phys*. 2020;127(15):150901.
- [3] Hussein MI, Leamy MJ, Ruzzene M. Dynamics of Phononic Materials and Structures: Historical Origins, Recent Progress, and Future Outlook. *Appl Mech Rev*. 2014;66(4):040802.
- [4] Bilal OR, Foehr A, Daraio C. Bistable metamaterial for switching and cascading elastic vibrations. *Proc Natl Acad Sci USA*. 2017;114(18):4603-6.
- [5] Bilal OR, Foehr A, Daraio C. Reprogrammable Phononic Metasurfaces. *Adv Mater*. 2017;29(39):1700628.
- [6] Haghpanah B, Ebrahimi H, Mousanezhad D, Hopkins J, Vaziri A. Programmable Elastic Metamaterials. *Adv Eng Mater*. 2016;18(4):643-9.
- [7] Foehr A, Bilal OR, Huber SD, Daraio C. Spiral-Based Phononic Plates: From Wave Beaming to Topological Insulators. *Phys Rev Lett*. 2018;120(20):205501.
- [8] Yang H, Xu J, Xiong Z, Lu X, Zhang R-Y, Li H, et al. Optically Reconfigurable Spin-Valley Hall Effect of Light in Coupled Nonlinear Ring Resonator Lattice. *Phys Rev Lett*. 2021;127(4):043904.
- [9] Liu Z, Zhang X, Mao Y, Zhu YY, Yang Z, Chan CT, et al. Locally Resonant Sonic Materials. *Science*. 2000;289(5485):1734-6.
- [10] Kushwaha MS, Halevi P, Dobrzynski L, Djafari-Rouhani B. Acoustic band structure of periodic elastic composites. *Phys Rev Lett*. 1993;71(13):2022-5.

- 
- [11] Meng H, Chronopoulos D, Fabro AT, Maskery I, Chen Y. Optimal design of rainbow elastic metamaterials. *Intl J Mech Sci.* 2020;165:105185.
- [12] Meng H, Chronopoulos D, Fabro AT, Elmadih W, Maskery I. Rainbow metamaterials for broadband multi-frequency vibration attenuation: Numerical analysis and experimental validation. *J Sound Vib.* 2020;465:115005.
- [13] Barnhart MV, Xu X, Chen Y, Zhang S, Song J, Huang G. Experimental demonstration of a dissipative multi-resonator metamaterial for broadband elastic wave attenuation. *J Sound Vib.* 2019;438:1-12.
- [14] Liu Z, Chan CT, Sheng P. Analytic model of phononic crystals with local resonances. *Phys Rev B.* 2005;71(1):014103.
- [15] Krushynska AO, Miniaci M, Bosia F, Pugno NM. Coupling local resonance with Bragg band gaps in single-phase mechanical metamaterials. *Extreme Mech Lett.* 2017;12:30-6.
- [16] Liu L, Hussein MI. Wave Motion in Periodic Flexural Beams and Characterization of the Transition Between Bragg Scattering and Local Resonance. *J Appl Mech.* 2012;79(1):011003.
- [17] Fei X, Jin L, Zhang X, Li X, Lu M. Three-dimensional anti-chiral auxetic metamaterial with tunable phononic bandgap. *Appl Phys Lett.* 2020;116(2):021902.
- [18] Muhammad. Design and manufacturing of monolithic mechanical metastructures governing ultrawide low frequency three-dimensional bandgaps. *Addit Manuf.* 2021;47:102231.
- [19] Park HW, Seung HM, Kim M, Choi W, Oh JH. Continuum flexural metamaterial for broadband low-frequency band gap. *Phys Rev Appl.* 2021;15(2):024008.
- [20] Yilmaz C, Hulbert GM, Kikuchi N. Phononic band gaps induced by inertial amplification in periodic media. *Phys Rev B.* 2007;76(5):054309.
- [21] Yilmaz C, Kikuchi N. Analysis and design of passive low-pass filter-type vibration isolators considering stiffness and mass limitations. *J Sound Vib.* 2006;293(1-2):171-95.
- [22] Delpero T, Hannema G, Damme BV, Schoenwald S, Zemp A, Bergamini A. Inertia Amplification in Phononic Crystals for Low Frequency Band Gaps. VIII ECCOMAS Thematic Conference on Smart Structures and Materials SMART 20172017. p. 1657-68.
- [23] Yilmaz C. Inertial Amplification Induced Phononic Band Gaps in a Chiral Elastic Metamaterial. 2018 12th International Congress on Artificial Materials for Novel Wave Phenomena (Metamaterials)2018. p. 451-3.
- [24] Orta AH, Yilmaz C. Inertial amplification induced phononic band gaps generated by a compliant axial to rotary motion conversion mechanism. *J Sound Vib.* 2019;439:329-43.
- [25] Bergamini A, Miniaci M, Delpero T, Tallarico D, Van Damme B, Hannema G, et al. Tacticity in chiral phononic crystals. *Nat Commun.* 2019;10(1):4525.
- [26] Xi C, Dou L, Mi Y, Zheng H. Inertial amplification induced band gaps in corrugated-core sandwich panels. *Compos Struct.* 2021;267:113918.
- [27] Banerjee A, Adhikari S, Hussein MI. Inertial amplification band-gap generation by coupling a levered mass with a locally resonant mass. *Intl J Mech Sci.* 2021;207:106630.
- [28] Yuksel O, Yilmaz C. Realization of an ultrawide stop band in a 2-D elastic metamaterial with topologically optimized inertial amplification mechanisms. *Int J Solids Struct.* 2020;203:138-50.
- [29] Taniker S, Yilmaz C. Generating ultra wide vibration stop bands by a novel inertial amplification mechanism topology with flexure hinges. *Int J Solids Struct.* 2017;106-107:129-38.
- [30] Yilmaz C, Hulbert GM. Theory of phononic gaps induced by inertial amplification in finite structures. *Phys Lett A.* 2010;374(34):3576-84.
- [31] Li J, Yang P, Li S. Multiple band gaps for efficient wave attenuation by inertial amplification in periodic functionally graded beams. *Compos Struct.* 2021;271:114130.
- [32] Krushynska AO, Amendola A, Bosia F, Daraio C, Pugno NM, Fraternali F. Accordion-like metamaterials with tunable ultra-wide low-frequency band gaps. *New J Phys.* 2018;20(7):073051.
- [33] Zheng B, Xu J. Mechanical logic switches based on DNA-inspired acoustic metamaterials with ultrabroad low-frequency band gaps. *J Phys D: Appl Phys.* 2017;50(46):465601.
- [34] Li J, Yang P, Li S. Phononic band gaps by inertial amplification mechanisms in periodic composite sandwich beam with lattice truss cores. *Compos Struct.* 2020;231:11458.
- [35] R E. The Corpuscular Theory of Matter. *Nature.* 1908;77(2005):505-6.
- [36] Jackson JD. *Classical electrodynamics.* New York: Wiley; 1998.
- [37] Wu W, Hu W, Qian G, Liao H, Xu X, Berto F. Mechanical design and multifunctional applications of chiral mechanical metamaterials: A review. *Mater Des.* 2019;180:107950.
- [38] Lakes R. Foam Structures with a Negative Poisson's Ratio. *Science.* 1987;235(4792):1038-40.
- [39] Baravelli E, Ruzzene M. Internally resonating lattices for bandgap generation and low-frequency vibration control. *J Sound Vib.* 2013;332(25):6562-79.

- 
- [40] Frenzel T, Kadic M, Wegener M. Three-dimensional mechanical metamaterials with a twist. *Science*. 2017;358(6366):1072-4.
- [41] Taylor M, Francesconi L, Gerendás M, Shanian A, Carson C, Bertoldi K. Low Porosity Metallic Periodic Structures with Negative Poisson's Ratio. *Adv Mater*. 2014;26(15):2365-70.
- [42] Yeh S-L, Harn RL. Origins of broadband vibration attenuation empowered by optimized viscoelastic metamaterial inclusions. *J Sound Vib*. 2019;458:218-37.
- [43] Pfeiffer C, Grbic A. Metamaterial Huygens' surfaces: tailoring wave fronts with reflectionless sheets. *Phys Rev Lett*. 2013;110(19):197401.
- [44] Huygens C. *Traite' de la Lumie're* (Pieter van der Aa, Leyden, 1690).
- [45] Lee U. **Spectral Element Method in Structural Dynamics**: John Wiley & Sons; 2009.
- [46] Phani AS, Woodhouse J, Fleck NA. Wave propagation in two-dimensional periodic lattices. *J Acous Soc Am*. 2006;119(4):1995-2005.
- [47] Matlack KH, Bauhofer A, Krödel S, Palermo A, Daraio C. Composite 3D-printed metastructures for low-frequency and broadband vibration absorption. *Proc Natl Acad Sci USA*. 2016;113(30):8386-90.
- [48] Miniaci M, Gliozzi AS, Morvan B, Krushynska A, Bosia F, Scalerandi M, et al. Proof of Concept for an Ultrasensitive Technique to Detect and Localize Sources of Elastic Nonlinearity Using Phononic Crystals. *Phys Rev Lett*. 2017;118(21):214301.
- [49] Chang Y-C, Schulman JN. Complex band structures of crystalline solids: An eigenvalue method. *Phys Rev B*. 1982;25(6):3975-86.
- [50] Kushwaha MS, Halevi P, Martínez G, Dobrzynski L, Djafari-Rouhani B. Theory of acoustic band structure of periodic elastic composites. *Phys Rev B*. 1994;49(4):2313-22.
- [51] Thomas JM. The birth of X-ray crystallography. *Nature*. 2012;491(7423):186-7.
- [52] Frandsen NMM, Bilal OR, Jensen JS, Hussein MI. Inertial amplification of continuous structures: Large band gaps from small masses. *J Appl Phys*. 2016;119(12):124902.
- [53] Ding W, Chen T, He Y, Chen C, Huang W, Jiang Z, et al. 3D syndiotactic elastic metastructure with single-phase material. *Phys Lett A*. 2020;384(35):126892.
- [54] Zeng Y, Cao L, Wan S, Guo T, An S, Wang Y-F, et al. Inertially amplified seismic metamaterial with an ultra-low-frequency bandgap. *Appl Phys Lett*. 2022;121(8):081701.